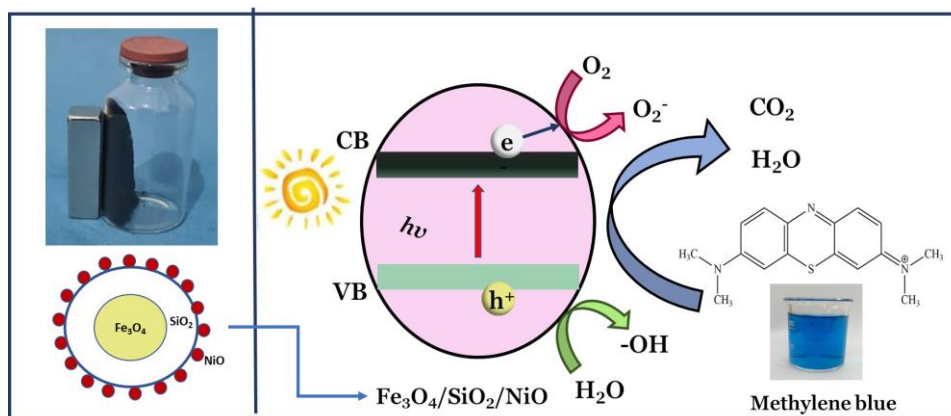


14 **Graphical Abstract**



15

16

17

18 **ABSTRACT**

19 Photocatalytic degradation for wastewater treatment is a method that has recently attracted attention.

20 In this research, a synthesized composite of $\text{Fe}_3\text{O}_4/\text{SiO}_2/\text{NiO}$ with magnetic properties was used for

21 the photocatalytic degradation of methylene blue dye under UV light. Furthermore, the composites

22 were characterized using XRD, FTIR, BET surface area, SEM-EDS, VSM, and UV-DRS. The results

23 showed that the $\text{Fe}_3\text{O}_4/\text{SiO}_2/\text{NiO}$ composite is magnetic with a saturation magnetization of 53.84

24 emu/g. The $\text{Fe}_3\text{O}_4/\text{SiO}_2/\text{NiO}$ composite has a surface area of 128.8 m^2/g , large than Fe_3O_4 and

25 $\text{Fe}_3\text{O}/\text{SiO}_2$. The $\text{Fe}_3\text{O}_4/\text{SiO}_2/\text{NiO}$ composite has a band gap of 2.83 eV. The photocatalytic activity of

26 $\text{Fe}_3\text{O}_4/\text{SiO}_2/\text{NiO}$ composite against the methylene blue dye exhibited high degradation efficiency

27 reaching 98.51 %. The pseudo-first-order is appropriate to describe the kinetics model of

28 photocatalytic degradation on methylene blue dye . The decrease in the degradation efficiency of the

29 $\text{Fe}_3\text{O}_4/\text{SiO}_2/\text{NiO}$ composite after 5 times for the photocatalytic degradation of methylene blue dye

30 from 98.02 % to 94.97 % indicates that the catalyst has high stability. Considering these results, the

31 $\text{Fe}_3\text{O}_4/\text{SiO}_2/\text{NiO}$ composites could be used as a potential catalyst in industrial wastewater.

32 **Keywords:** $\text{Fe}_3\text{O}_4/\text{SiO}_2/\text{NiO}$, magnetic composite, photocatalytic, degradation, methylene blue dye

33 1. Introduction

34 Wastewater discharged from industry often contains pathogenic organisms in organic and
35 inorganic contaminants that harm the environment (Pham *et al.*, 2018). It contains dyes with several
36 characteristics, including a large volume of waste, high chromaticity, high organic matter
37 concentration, poor biodegradability, disturbing aesthetics, and blocking the transmission of sunlight,
38 thereby reducing the photosynthetic activity in the waters. Additionally, a low concentration of dye
39 (< 1 mg/L) can disturb the waters (Vandevivere *et al.*, 1998). Methylene blue ($C_{16}H_{18}ClN_3S$) is a
40 cationic dye widely used in the coloring industry and as a chemical indicator (Khodai *et al.*, 2013;
41 Kuang *et al.*, 2020). It has an aromatic group and a complex structure that is hydrophilic and stable
42 to light, temperature, and chemicals (Hou *et al.*, 2018).

43 Various technologies, such as biological, physical, and chemical treatment have been used to
44 reduce the concentration of dyes. The methods used to removal dye include adsorption (Ziaadini *et*
45 *al.*, 2019), precipitation (Ali *et al.*, 2006), coagulation-flocculation (Moghaddam *et al.*, 2010),
46 filtration (David *et al.*, 2020), ozonation (Dias *et al.*, 2019) and others. Adsorption is often applied
47 because it effectively reduces the concentration of dyes but causes secondary pollutants (Fu *et al.*,
48 2019). Presently, Advanced Oxidation Processes (AOPs) have been an effective method for
49 degrading organic pollutants (Behzadi *et al.*, 2020) due to their low cost and high efficiency (Behzadi
50 *et al.*, 2020; Jarariya, 2022).

51 The AOPs method often used is heterogeneous photocatalysis based on semiconductor
52 materials. The irradiation of the semiconductor by photons on the band gap energy produces positive
53 and negative electrons. Furthermore, the positive hole reacts with a water molecule to produce a
54 hydroxyl radical ($\bullet OH$), while electrons react with O_2 molecules to form superoxide radicals ($\bullet O_2$).
55 The hydroxyl and superoxide radicals degrade dye into smaller non-toxic compounds, CO_2 and H_2O
56 (Gao *et al.*, 2013; Salomon *et al.*, 2012). The several semiconductor materials used include TiO_2 (Hou
57 *et al.*, 2018), $NiFe_2O_4$ (Hariani *et al.*, 2021), NiO (Lett *et al.*, 2022), ZnO (Chen *et al.*, 2017), and
58 $CoFe_2O_4$ (Loan *et al.*, 2019).

59 Nickel oxide (NiO) is a p-type transition metal oxide semiconductor with a band gap of about
60 3.5 eV, antiferromagnetic, high conductivity, stable, and catalytic properties (Hosny, 2011; D'Amario
61 *et al.*, 2018; Barakat *et al.*, 2013). It performs effectively in the photodegradation of orange II dye
62 (Khan *et al.*, 2022), methylene blue (Let *et al.*, 2022; Wan *et al.*, 2013), and methyl orange dye
63 (Barzinjy *et al.*, 2020). The combination of magnetic ferrite with NiO is a strategy to increase the
64 efficiency of the catalytic process and the separation of the catalyst from the solution. The magnetic
65 ferrite serves as a core. SiO₂ is a layer to avoid the interaction between NiO and magnetic ferrite. The
66 core-shell-shell structure increases the surface area, reduces the cost of catalyst usage, and increases
67 lifespan (Channei *et al.*, 2014; Girginova *et al.*, 2010). For example, Fe₃O₄ coated with activated
68 carbon and TiO₂ showed better catalytic ability than used with only TiO₂ (Gebrezgiabher *et al.*, 2019).

69 This research synthesized a magnetic composite of Fe₃O₄/SiO₂/NiO, with Fe₃O₄ as the core,
70 SiO₂ as the inner shell, and NiO as the outer shell. Fe₃O₄ is the most widely used magnetic iron oxide
71 compared to other ferrite compounds with an inverse spinel structure and superparamagnetic. The
72 advantage of using Fe₃O₄ as a core in composites, after being used for photocatalytic degradation
73 process, the composite can easily be separated from the solution using an external magnet, without
74 filtering. Fe₃O₄/SiO₂/NiO were applied for photocatalytic degradation of methylene blue dye under
75 UV light irradiation. Finally, the kinetic photocatalytic degradation and reusability of these
76 composites were investigated.

77 **2. Materials and methods**

78 *2.1. Materials*

79 The materials used are of analytical grade without purification, including FeCl₂·4H₂O,
80 FeCl₃·6H₂O, NiCl₂·6H₂O, NaOH, HCl, C₂H₅OH, NH₄OH, NH₄HCO₃, Tetraethyl
81 orthosilicate (TEOS), Diethylene Glycol (DEG), methylene blue dye purchased from Merck
82 (Germany), distilled water, and N₂ gas.

83

84

85 2.2. Synthesis of Fe_3O_4

86 Fe_3O_4 was synthesized using the coprecipitation method. First, a total of 1.988 g $FeCl_2 \cdot 4H_2O$
87 and 5.406 g $FeCl_3 \cdot 6H_2O$ were dissolved in 20 mL of distilled water. Afterward, 1 M NaOH was added
88 to the solution dropwise while slowly stirring with a magnetic stirrer at a speed of 100 rpm, and N_2
89 gas was emitted until the pH reached ± 10 . The precipitate was separated from the solution using a
90 magnet and washed several times with distilled water and ethanol until the pH was neutral. Finally,
91 it was dried in an oven at $70^\circ C$ for 3 hours.

92 2.3. Synthesis of Fe_3O_4/SiO_2

93 The Fe_3O_4/SiO_2 was synthesized using the Stober method. First, 0.5 g Fe_3O_4 was dispersed in
94 20 mL of ethanol using an ultrasonic bath for 30 minutes at room temperature. The obtained product
95 was added 5 mL of ammonia solution (28%), followed by the gradual addition of 2 mL TEOS solution
96 (1 mL TEOS in 20 mL ethanol) using a magnetic stirrer for 3 for 5 hours. The precipitate was washed
97 several times with distilled water and ethanol until the pH was neutral. The Fe_3O_4/SiO_2 were dried in
98 an oven at a temperature of $70^\circ C$ for 3 hours.

99 2.4. Synthesis of $Fe_3O_4/SiO_2/NiO$

100 An amount of 0.5 g of $NiCl_2 \cdot 6H_2O$ was dispersed in 10 mL of DEG for 30 minutes at room
101 temperature using a water bath sonicator, followed by adding 0.5 g of Fe_3O_4/SiO_2 and 10 mL of
102 0.0025 M NH_4HCO_3 solution under stirring for 15 minutes. The mixture was transferred to a Teflon
103 autoclave and heated at 120 for 5 hours. The precipitate was washed using distilled water and ethanol.
104 The obtained product was dried in an oven at $70^\circ C$ for 3 hours. Finally, it is calcined at a temperature
105 of $300^\circ C$ for 2 hours.

106 2.5. Characterization

107 The product obtained was identified using an X-ray diffractometer (XRD Panalytical), operated
108 at 40 kV and 30 mA, $Cu\alpha$ ($\lambda = 1.542 \text{ \AA}$) as a radiation source, and a range of 2θ at $10-90^\circ$. The bond
109 formation was analyzed with Fourier Transform Infra-Red spectroscopy (FTIR, Prestige 21,
110 Shimadzu) at wave numbers of $400-4000 \text{ cm}^{-1}$ using the KBr pellet technique. Furthermore, the

111 specific surface areas were evaluated with N₂ adsorption-desorption using the BET (Quantachrome
112 QuadraWin) method. Scanning electron microscopy with an energy dispersive spectrometer (SEM-
113 EDS JSM 6510) was used to observe surface morphology and elemental composition. Additionally,
114 magnetic properties were evaluated using a Vibrating Sample Magnetometer (VSM Oxford Type 1.2
115 T). UV-Vis Diffuse Reflectance Spectroscopy (Pharmaspec, UV-1700) was used to determine the
116 band gap at 200-800 nm wavelengths. The concentration of methylene blue dye was determined using
117 a UV-Vis spectrophotometer (Type Orion Aquamate 8000).

118 2.6. Photocatalytic activity

119 Photocatalytic activity of Fe₃O₄/SiO₂/NiO against methylene blue dye under UV light
120 irradiation source (15-W x 3, Philips). In the experiment, 50 mL methylene blue dye at a concentration
121 of 20 mg/L with a 0.5 g/L catalyst dose, the pH of the solution was varied at 5, 6, 7, 8, 9, and 10 using
122 0.1 M HCl or NaOH. The mixture was stirred in a dark room for 40 minutes to reach equilibrium,
123 followed by a photocatalytic degradation process for 120 minutes (20 minutes intervals). Other
124 variables are catalyst dose (0.25, 0.5, 0.75 and 1.0 g/L) and the dye concentration (10, 20, 30, and 40
125 mg/L).

126 The reusability of the catalyst was assessed by magnetically separating it following photocatalytic
127 degradation under optimal conditions. It was then washed using deionized water and dried in an oven
128 for 3 hours at 70°C. Calcination was carried out at 300°C for ± 2 hours to remove organic substances
129 (Prasad *et al.*, 2022). Finally, the catalyst is reused for photocatalytic degradation and repeated up to
130 5 times.

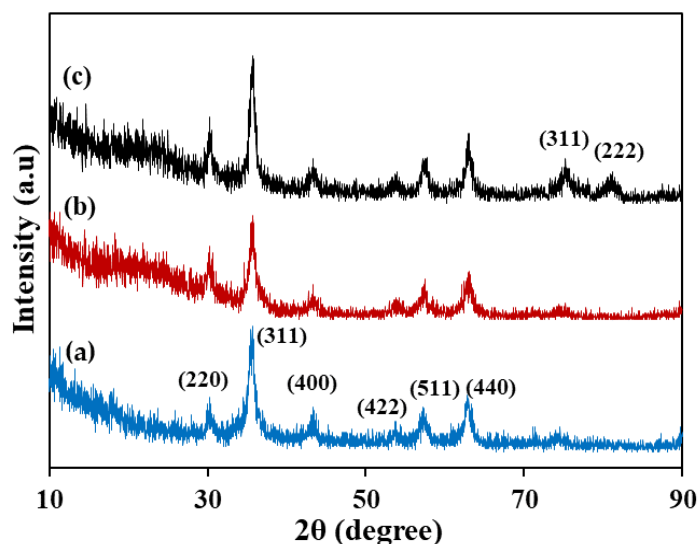
131 3. Results and Discussion

132 3.1. Catalyst characterization

133 Fe₃O₄ as the core was synthesized and coated SiO₂ using the coprecipitation and the sol-gel
134 methods, respectively. The Fe₃O₄/SiO₂/NiO was synthesized using the hydrothermal technique.
135 Figure 1 shows that the crystal structure of Fe₃O₄, Fe₃O₄/SiO₂, and Fe₃O₄/SiO₂/NiO were determined
136 using XRD. According to the cubic spinel phase (JCPDS card no. 74-0748), the diffraction

137 characteristics of Fe_3O_4 were observed at $2\theta = 30.39^\circ, 35.69^\circ, 43.35^\circ, 53.87^\circ, 57.65^\circ,$ and 62.97° .
138 This was appropriate for the planes (220), (311), (400), (422), (511), and (440). After coating with
139 SiO_2 , a broad peak was observed at 2θ around 23° . This peak is a characteristic of amorphous SiO_2
140 (Chen *et al.*, 2014).

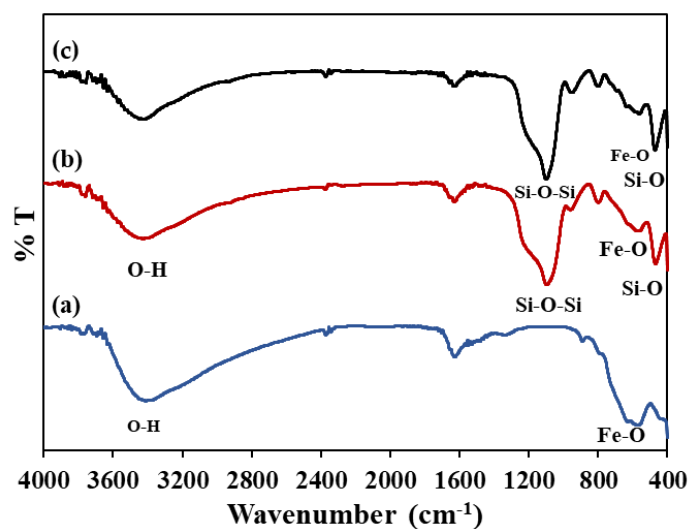
141 The new peaks in $\text{Fe}_3\text{O}_4/\text{SiO}_2/\text{NiO}$ were observed at $2\theta = 76.01^\circ$ (311) and 80.05° (222).
142 Meanwhile, other peaks overlapped those of Fe_3O_4 , including 37.21° (111), 43.45° (200), and 62.95°
143 (220), according to the structure of JCPDS card no. 78-0423 (NiO). Using the Debye-Scherrer
144 equation, the crystal size of Fe_3O_4 was calculated to be 7.0 nm, while those of $\text{Fe}_3\text{O}_4/\text{SiO}_2$ and
145 $\text{Fe}_3\text{O}_4/\text{SiO}_2/\text{NiO}$ were 8.2 nm. Another research showed that coating Fe_3O_4 with SiO_2 increased the
146 crystal size from 22.60 to 38.0 nm (Reman *et al.*, 2021).



147
148 **Figure 1.** XRD diffraction pattern of (a) Fe_3O_4 , (b) $\text{Fe}_3\text{O}_4/\text{SiO}_2$, and (c) $\text{Fe}_3\text{O}_4/\text{SiO}_2/\text{NiO}$

149 Figure 2 shows the FTIR spectra of Fe_3O_4 , $\text{Fe}_3\text{O}_4/\text{SiO}_2$, and $\text{Fe}_3\text{O}_4/\text{SiO}_2/\text{NiO}$. The wave
150 numbers between 3400 cm^{-1} and 1600 cm^{-1} appear in all peaks, indicating the presence of O-H groups
151 from free water, which is absorbed by the catalyst (Hariani *et al.*, 2021; Elzahrani 2017; Ojemaye *et*
152 *al.*, 2017). In Figure 2(a), Fe-O stretching vibration is observed at a wave of 557.43 cm^{-1} . Meanwhile,
153 no other peak was observed apart from water absorption. Figure 2b shows an additional peak at 464.84
154 and 804.31 cm^{-1} , which indicates symmetrical and asymmetrical Si-O terminals (Reman *et al.*, 2021).
155 A strong peak at 1089.78 cm^{-1} is an asymmetric Si-O-Si and Si-O-H vibrational bond observed at a

156 wave number of 950.60 cm^{-1} (Fu *et al.*, 2019; Han and An, 2021). The wave number for metal-oxygen
157 stretching vibration was observed in the $400\text{--}700\text{ cm}^{-1}$ range. The absorption band in the $600\text{--}700$
158 cm^{-1} indicates absorptions of Ni-O stretching vibration. This study appears at 670.32 cm^{-1} , even
159 though it is not sharp (Qiao *et al.*, 2009).

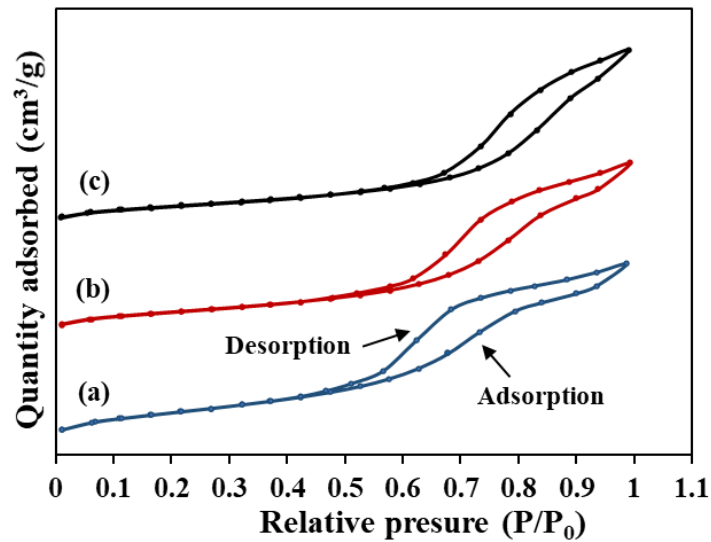


160

161 **Figure 2.** FTIR spectra of (a) Fe_3O_4 , (b) $\text{Fe}_3\text{O}_4/\text{SiO}_2$, and (c) $\text{Fe}_3\text{O}_4/\text{SiO}_2/\text{NiO}$

162 The surface area affects the catalyst's ability in the degradation process (Kalam *et al.*, 2018).
163 Based on the N_2 gas adsorption-desorption curve shown in Figure 3, the specific surface area (S_{BET})
164 of Fe_3O_4 , $\text{Fe}_3\text{O}_4/\text{SiO}_2$, and $\text{Fe}_3\text{O}_4/\text{SiO}_2/\text{NiO}$ were determined using BET analysis. According to the
165 classification IUPAC, all BET curves showed compliance with the Type IV isotherm, namely
166 mesoporous materials. The specific surface area of Fe_3O_4 (S_{BET}) is $88.4\text{ m}^2/\text{g}$, but after coating with
167 SiO_2 , it becomes $124.2\text{ m}^2/\text{g}$. SiO_2 protects it from agglomeration processes, thereby increasing the
168 surface area (Li *et al.*, 2017; Wu *et al.*, 2020). Another research showed that coating Fe_3O_4 with
169 graphene oxide (GO) produces a larger surface area than Fe_3O_4 and GO (Thy *et al.*, 2020). In this
170 study, the $\text{Fe}_3\text{O}_4/\text{SiO}_2/\text{NiO}$ has a larger surface area than Fe_3O_4 and $\text{Fe}_3\text{O}_4/\text{SiO}_2$, which are $128.8\text{ m}^2/\text{g}$.
171 These results are similar to $\text{CoFe}_2\text{O}_4/\text{SiO}_2/\text{TiO}_2$, which have a larger surface area than CoFe_2O_4 and
172 $\text{CoFe}_2\text{O}_4/\text{SiO}_2$ (Zielińska-Jurek *et al.*, 2017).

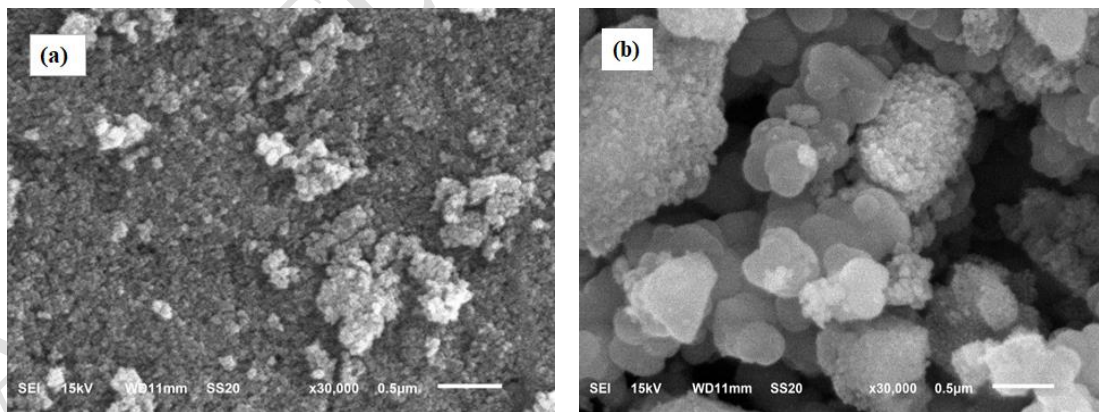
173



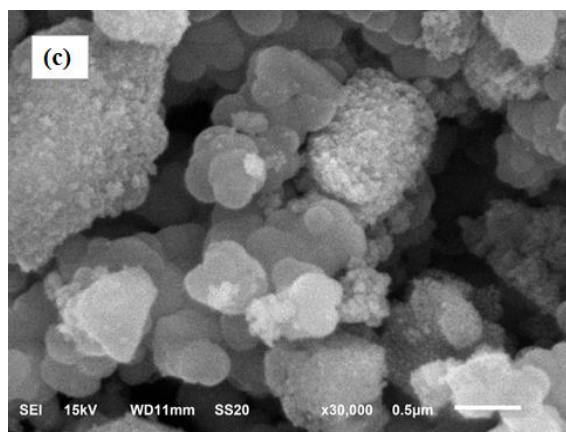
174

175 **Figure 3.** N₂ adsorption-desorption isotherm of (a) Fe₃O₄, (b) Fe₃O₄/SiO₂, and (c) Fe₃O₄/SiO₂/NiO

176 Figure 4 presents the morphology of Fe₃O₄, Fe₃O₄/SiO₂, and Fe₃O₄/SiO₂/NiO analyzed using
 177 SEM. The Fe₃O₄ surface appears to be small, dense, and agglomerated, while the Fe₃O₄/SiO₂ and
 178 Fe₃O₄/SiO₂/NiO appear to be a granular molecule with reasonably large sizes coating Fe₃O₄. The
 179 SEM mapping of the Fe₃O₄/SiO₂/NiO in Figure 5 shows the distribution of elements on the composite
 180 surface. Some parts of the surface indicate the agglomeration of Fe₃O₄ (red). Meanwhile, Ni (blue)
 181 appears to be distributed on the surface of Fe₃O₄/SiO₂ and Fe₃O₄.



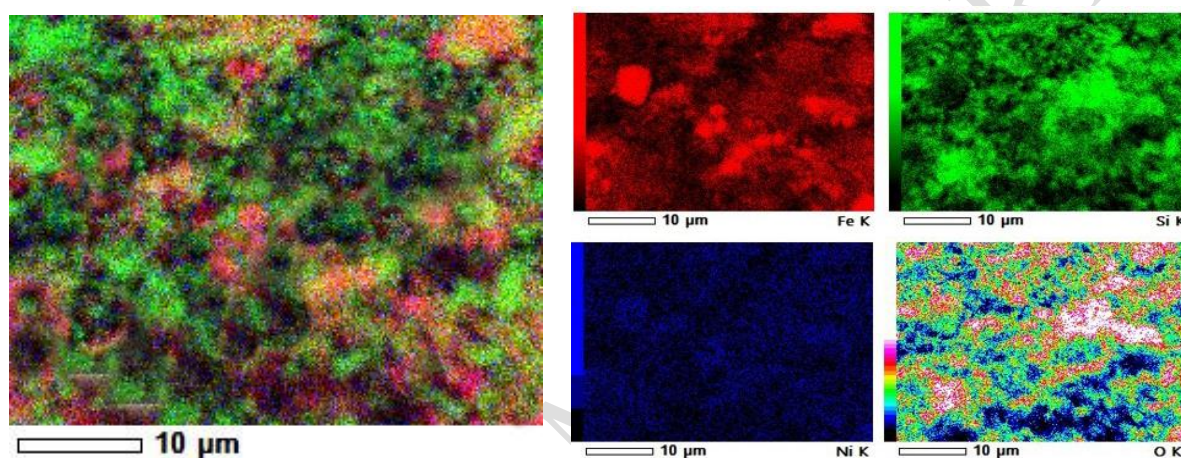
182



183

184

Figure 4. Morphology of (a) Fe_3O_4 , (b) $\text{Fe}_3\text{O}_4/\text{SiO}_2$, and (c) $\text{Fe}_3\text{O}_4/\text{SiO}_2/\text{NiO}$



185

186

Figure 5. SEM Mapping of $\text{Fe}_3\text{O}_4/\text{SiO}_2/\text{NiO}$

187

188

189

190

Table 1 shows the composition of Fe_3O_4 , $\text{Fe}_3\text{O}_4/\text{SiO}_2$, and $\text{Fe}_3\text{O}_4/\text{SiO}_2/\text{NiO}$ as a result of EDX analysis. The composition of Fe_3O_4 consists of Fe and O, which indicates its purity. The addition of Si to $\text{Fe}_3\text{O}_4/\text{SiO}_2$ indicates that SiO_2 has successfully coated Fe_3O_4 , while the addition of Ni shows that the element was distributed on the surface of $\text{Fe}_3\text{O}_4/\text{SiO}_2$.

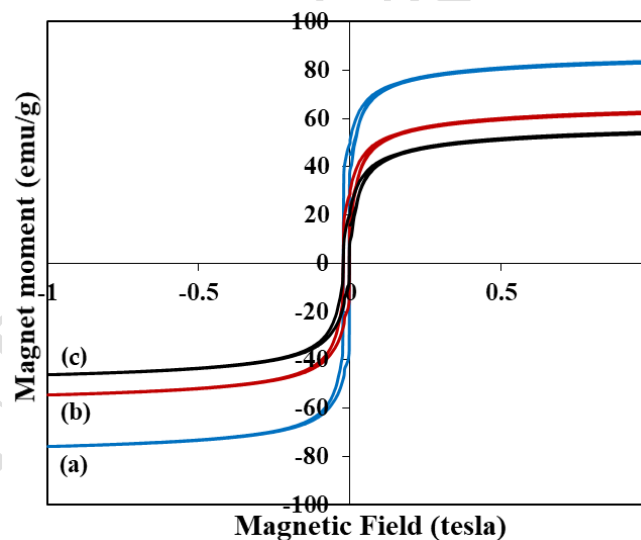
191

Table 1. EDX analysis of Fe_3O_4 , $\text{Fe}_3\text{O}_4/\text{SiO}_2$, and $\text{Fe}_3\text{O}_4/\text{SiO}_2/\text{NiO}$

Materials	Elements (%)			
	O	Fe	Si	Ni
Fe_3O_4	29.70	70.30	-	-
$\text{Fe}_3\text{O}_4/\text{SiO}_2$	53.51	18.60	27.89	-
$\text{Fe}_3\text{O}_4/\text{SiO}_2/\text{NiO}$	53.28	14.64	23.97	8.11

192

193 Figure 6 shows the magnetic properties of Fe_3O_4 , $\text{Fe}_3\text{O}_4/\text{SiO}_2$, and $\text{Fe}_3\text{O}_4/\text{SiO}_2/\text{NiO}$. The Fe_3O_4
194 saturation magnetization of 83.26 emu/g is classified as strong magnetization. Previous research
195 showed that nanomagnetic coating ferrite with non-magnetic materials reduces saturation
196 magnetization. Subsequently, coating Fe_3O_4 with SiO_2 blocks the interaction of the magnetic dipole
197 between adjacent magnetic particles and isolates them from the magnetic field (Kotutha *et al.*, 2019).
198 In general, SiO_2 is non-magnetic, which implies that it is insulating and inert. In this research, the
199 saturation magnetization values of $\text{Fe}_3\text{O}_4/\text{SiO}_2$ and $\text{Fe}_3\text{O}_4/\text{SiO}_2/\text{NiO}$ were 61.96 and 53.84 emu/g,
200 respectively. The presence of NiO reduces the properties of $\text{Fe}_3\text{O}_4/\text{SiO}_2$. This is related to the surface
201 effect and anisotropy of the particles (Zhao *et al.*, 2015; Sadeghi *et al.*, 2012). The magnetization
202 curve shows a mixture of ferromagnetic and superparamagnetic properties. Therefore, the magnetic
203 properties allow for the easy separation of the composite from the solution after being used for
204 photocatalytic degradation.



205
206 **Figure 6.** The magnetization of (a) Fe_3O_4 , (b) $\text{Fe}_3\text{O}_4/\text{SiO}_2$ and (c) $\text{Fe}_3\text{O}_4/\text{SiO}_2/\text{NiO}$

207 The energy absorbed by the catalyst depends on the optical band gap energy, namely the
208 difference between the valence and conduction bands (Kalam *et al.*, 2018). Figure 7 shows plots
209 $(\alpha h\nu)^2$ versus Energy (eV) to obtain band gap values of $\text{Fe}_3\text{O}_4/\text{SiO}_2/\text{NiO}$. The broad spectrum
210 indicates that Fe_3O_4 dominates the phase in the material. Finally, the band gap value is obtained from
211 Tauc's plot according to the following equation.

212

$$(\alpha h\nu)^2 = A(h\nu - E_g) \quad (1)$$

213

214

215

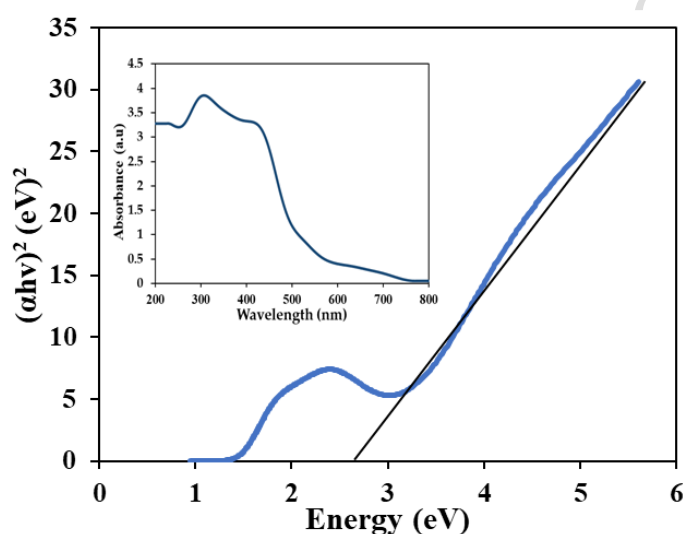
216

217

218

219

Where α , A , h , ν , and E_g are the absorption coefficient, proportionality constant, Planck's constant, vibrational frequency, and energy band gap. NiO was absorbed in a wavelength of 320 nm. Another research showed that NiO and Fe₃O₄ were observed at 330 nm and 440 nm, respectively (Barzinjy *et al.*, 2020). In this research, the Fe₃O₄/SiO₂/NiO band gap was 2.83 eV, which is smaller than the band gap of NiO ~ 3.5 eV and larger than the band gap of ferrite compounds ~ 2 eV (Hariani *et al.*, 2021). The formation of the core-shell-shell, namely the Fe₃O₄/SiO₂/NiO, successfully reduced the band gap.



220

221

Figure 7. Wood-Tauc plot for Fe₃O₄/SiO₂/NiO

222

3.2. Photocatalytic activity

223

224

225

226

227

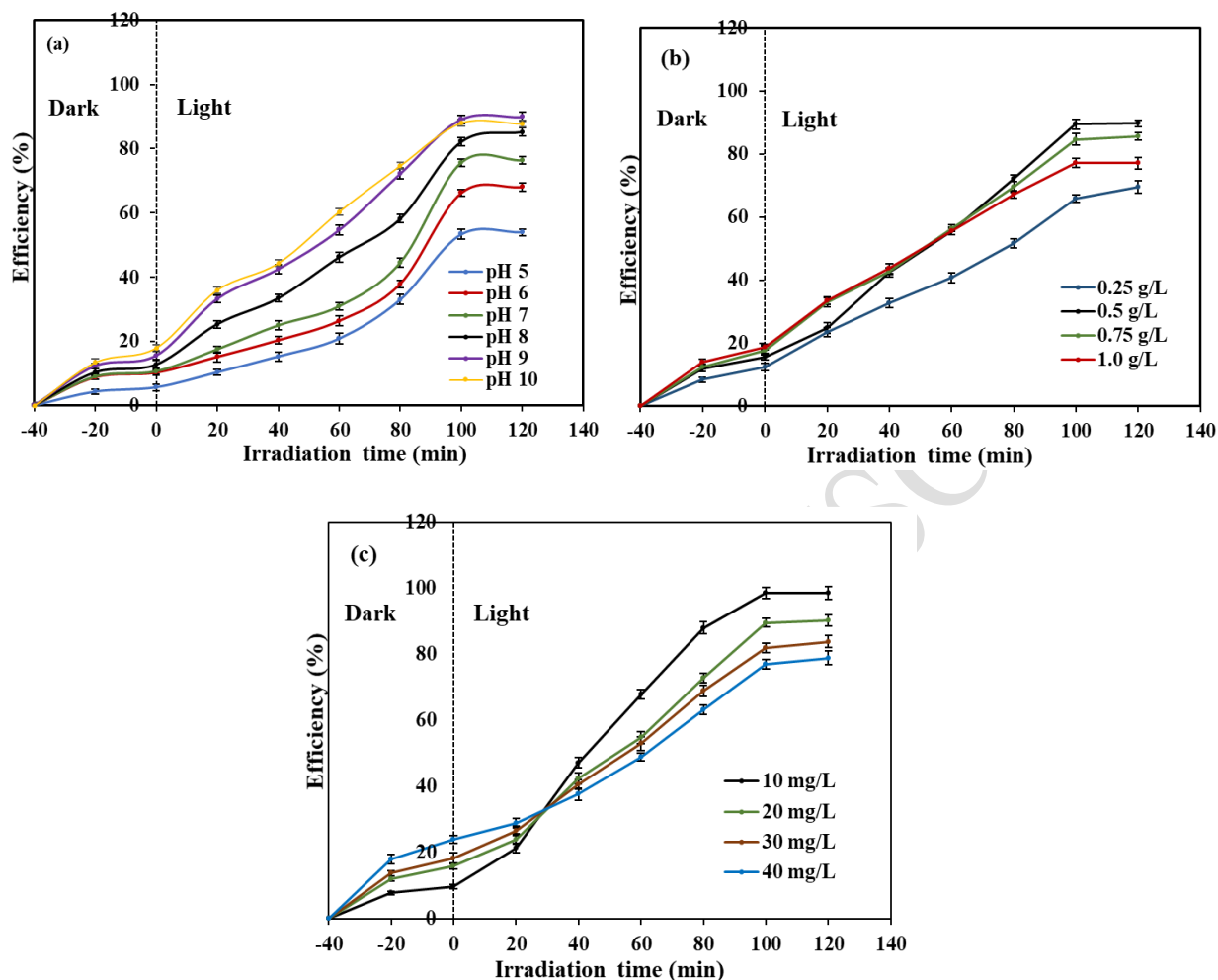
228

229

230

Figure 8a shows the effect of pH on the efficiency of photocatalytic degradation. The dye concentration was 20 mg/L, and the catalyst dose was 0.5 g/L with a pH varying from 5 to 10. The pH solution contributes to the degradation of dyestuffs and gives a charge to the catalyst's surface. Photocatalytic degradation of methylene blue dye using several catalysts, namely TiO₂, ZnO, Co₃O₄, CdS, and MnTiO₃, was optimum at a pH range of 9 to 11 (Alkaykh *et al.*, 2020; Alkaim *et al.*, 2014). Methylene blue dye is a cationic dye at alkaline pH, the dye has a positive charge, and the interaction is more effective with a negatively charged catalyst. Furthermore, there are many OH⁻ ions at the pH of alkaline solutions. The catalyst absorbs irradiation to produce holes (h_{VB}^+) which then react with

231 OH⁻ to form hydroxyl radicals (\bullet OH). At high pH, hydroxyl radicals are quickly scavenged, giving
232 them no opportunity to react with dyes (Alkaim *et al.*, 2014).



233

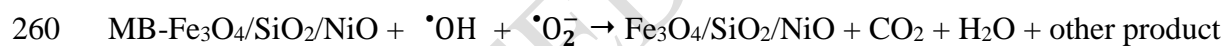
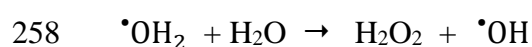
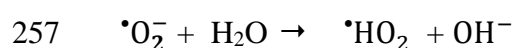
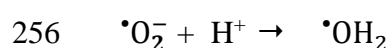
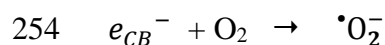
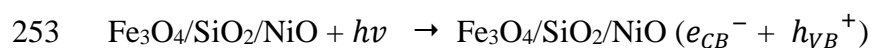
234

235 **Figure 8.** Effect of (a) pH solution, (b) catalyst dose, and (c) initial concentration of dye on the
236 photocatalytic degradation of the Fe₃O₄/SiO₂/NiO

237 The effect of catalyst doses was conducted with variations of 0.25, 0.5, 0.75, and 1.0 g/L, while
238 the concentration was 20 mg/L at a pH of 9. Figure 8b shows that the higher the amount of catalyst,
239 the more the dye degraded. In addition to being observed at 100 minutes, doses of 0.5 and 0.75 g/L
240 had nearly the same degradation rate. However, there was a decrease at 1.0 g/L. At higher doses, there
241 is a reduction in the reaction rate due to catalyst loading, which causes the deactivation of activated
242 molecules by collision with ground state catalysts (Herman, 1995). Furthermore, the optimum dose
243 was at 0.5 g/L with a dye reduction efficiency of 89.77% in 100 minutes.

244 The effect of the initial dye concentration was analyzed using 10 to 50 mg/L. Figure 8c shows
 245 that the dye reduction efficiency increased directly with the initial dye concentration after 100 min.
 246 It also increases with the number of dye molecules adsorbed on the catalyst surface. This prevents
 247 photons from reaching the catalyst surface as they are blocked by the dye (Hariani *et al.*, 2022;
 248 Makeswari and Saraswathi, 2020). Therefore, the photocatalytic degradation of methylene blue dye
 249 was better at a low concentration of 10 mg/L with an efficiency of 98.51%. This indicates that the
 250 catalyst plays a significant role in dye degradation.

251 The mechanism of photocatalytic degradation of methylene blue (MB) dye using Fe₃O₄/SiO₂/NiO
 252 composite according to the reaction: (Ammar *et al.*, 2020).

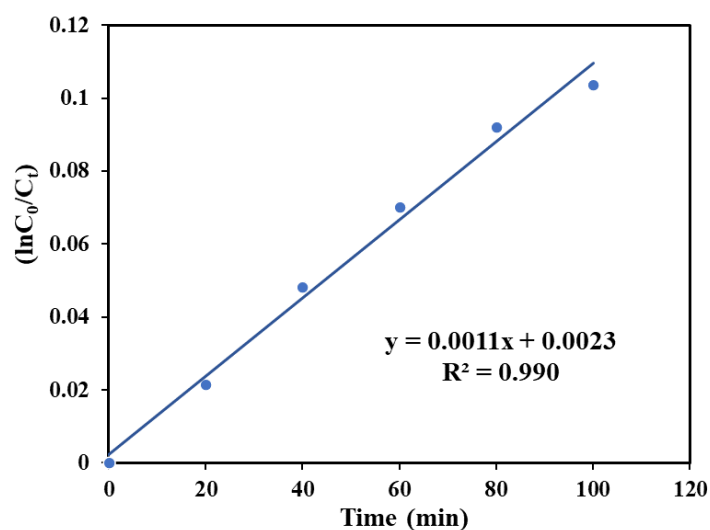


261 3.3. Kinetic for photodegradation

262 The following formula expresses the kinetic model of photocatalytic degradation on methylene
 263 blue dye using pseudo-first-order:

$$264 \ln C_0/C_t = kt \quad (2)$$

265 Where C_0 and C_t are the initial concentration at each time (a certain time) (mg/L), t is the irradiation
 266 time (min), and k is the rate constant (min⁻¹). The k value is obtained from the slope of the linear
 267 fitting graph $\ln C_0/C_t$ Versus t . This research determined the kinetics of photocatalytic degradation
 268 using a methylene blue dye concentration of 10 mg/L, a catalyst dose of 0.5 g/L, and a solution pH
 269 of 9 (Figure 9). The coefficient of determination value ($R^2 = 0.990 > 0.9$) indicates that the kinetic
 270 model is compatible (Van *et al.*, 2019). Therefore, the k value obtained is $1.1 \cdot 10^{-4} \text{ min}^{-1}$.



271

272 **Figure 9.** The plot of the pseudo-first-order for photocatalytic degradation on methylene blue dye

273 **3.4. Reusability of $Fe_3O_4/SiO_2/NiO$**

274 Reusability is essential for the remediation process as it aims to see the cost-effectiveness and
 275 feasibility of catalysts (Gebrezgiabher *et al.*, 2019; Moosavi *et al.*, 2020). Its performance uses
 276 methylene blue dye concentration of 10 mg/L, a dose of 0.5 g/L, and a solution of pH 9. Figure 10
 277 shows the efficiency of photocatalytic degradation after 5 cycles. Subsequently, the efficiency of
 278 photocatalytic degradation decreased from 98.02 to 94.97% (< 5%). The photocatalyst properties,
 279 such as surface area, number of active sites, and the presence of impurities, could change during
 280 reuse, but those with approximately 5 cycles continue to show good performance. It can be believed
 281 that the $Fe_3O_4/SiO_2/NiO$ exhibits excellent photocatalyst stability.

282

283

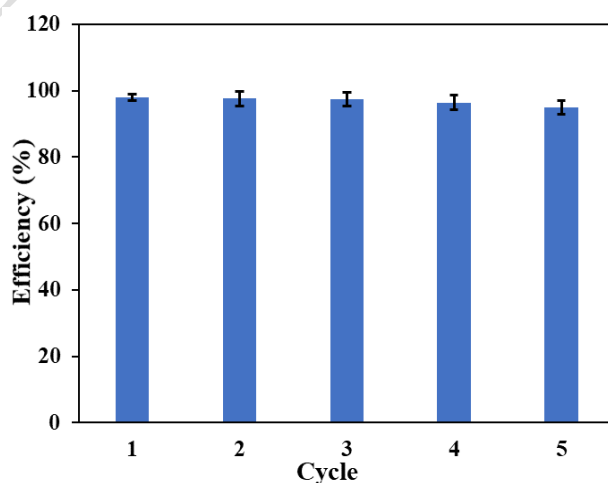


Figure 10. Reusability of $Fe_3O_4/SiO_2/NiO$

284 Table 2 shows a degradation efficiency comparison of methylene blue dye using several catalysts.
 285 The results of this research have high degradation efficiency with the same initial concentration and
 286 relatively fast time.

287 **Table 2.** Photocatalytic degradation efficiency of some catalysts against methylene blue dye

Catalyst	Initial concentration (mg/L)	Irradiation time (min)	Efficiency (%)	References
Cu-TiO ₂ /ZnO	35	120	64.72	Khaki <i>et al.</i> , (2017)
SnS ₂ -SiO ₂ @ α -Fe ₂ O ₃	5	100	96.0	Balu <i>et al.</i> , (2018)
ZnO-SnO ₂	10	60	96.53	Lin <i>et al.</i> , (2018)
TiO ₂ /Alg/FeNPs	5	120	97.6	Kanakaraju <i>et al.</i> , (2018)
CoFe ₂ O ₄ /H ₂ O ₂	10	140	82.0	Kalam <i>et al.</i> , (2018)
Fe ₃ O ₄ @SiO ₂ @CeO ₂	10	50	98.0	Ziaadini <i>et al.</i> , (2019)
CoFe ₂ O ₄ @SiO ₂ @DyCe ₂ O ₇	20	30	94.5	Zinatloo-Ajabshir and Salavati-Niasari (2019)
Fe ₂ TiO ₅	10	250	97.0	Vasiljevic <i>et al.</i> , (2020)
Fe ₃ O ₄ /SiO ₂ /NiO	10	100	98.51	Present study

288

289 4. Conclusion

290 The core-shell-shell composite Fe₃O₄/SiO₂/NiO has been successfully synthesized, with Fe₃O₄
 291 as the core, SiO₂ as the interlayer, and NiO spread on the composite surface. The composite has
 292 magnetic properties with a saturation magnetization value of 53.84 emu/g. Furthermore, the optimum
 293 conditions for photocatalytic degradation of Fe₃O₄/SiO₂/NiO against methylene blue dye were pH 9,
 294 catalyst dose of 0.5 g/L, 10 mg/L dye concentration, and irradiation time of 100 minutes, the

295 degradation efficiency of 98.51%. This composite has high stability, and reusability of approximately
296 5 cycles decreases the removal efficiency by < 5%. Therefore, the Fe₃O₄/SiO₂/NiO composite has the
297 potential to reduce water pollution. Further research needs to be developed for the photocatalytic
298 degradation of wastewater containing other pollutants.

299 **Acknowledgements**

300 This research was funded by the Ministry of Education, Culture, Research and Technology for
301 providing funding assistance through the *Penelitian Dasar Unggulan Perguruan Tinggi* (PDUPT) in
302 2022 as additional research output. Contract No. 0063.01/UN9.3.1/PL/2022.

303 **References**

304 Ali M., Sarkar A., Pandey M.D. and Pandey S. (2006), Efficient precipitation of dyes from dilute
305 aqueous solutions of ionic liquids, *Analytical sciences*, **22**, 1051–1053.

306 Alkaim A.F., Aljeboree A.M., Alrazaq N.A., Baqir S.J., Hussein F.H. and Lili A.J. (2014), Effect of
307 pH on adsorption and photocatalytic degradation efficiency of different catalyst on removal of
308 Methylene blue, *Asian Journal of Chemistry*, **26**, 8445–8448.

309 Alkaykh S., Mbarek A. and Ali-Shattle E.E. (2020), Photocatalytic degradation of methylene blue
310 dye in aqueous solution by MnTiO₃ nanoparticles under sunlight irradiation, *Heliyon*, **6**, 1–6.

311 Ammar S.H., Elaibi A.I., and Mohamme I.S. (2020), Core/shell Fe₃O₄@Al₂O₃-PMo magnetic
312 nanocatalyst for photocatalytic degradation of organic pollutants in an internal loop airlift reactor,
313 *Journal of Water Process Engineering*, **37**, 1–11

314 Balu S, Uma K., Pan G.T., Yang T.C. and Ramaraj S.K. (2018), Degradation of methylene blue dye
315 in the presence of visible light using SiO₂@ α -Fe₂O₃ nanocomposites deposited on SnS₂ flowers,
316 *Materials*, **6**, 1030.

317 Barakat A., Al-Noaimi M., Suleiman M., Aldwayyan A.S., Hammouti B., Hadda T.B., Haddad S.F.,
318 Boshala A. and Warad I. (2013), One Step Synthesis of NiO Nanoparticles via Solid-State

- 319 Thermal Decomposition at Low-Temperature of Novel Aqua (2,9-dimethyl-1,10-
320 phenanthroline) NiCl₂ Complex, *International Journal of Molecular Sciences*, **14**, 23941–23954.
- 321 Barzinjy A.A., Hamad S.M., Aydin S., Ahmed M.H. and Hussain F.H.S. (2020), Green and eco-
322 friendly synthesis of Nickel oxide nanoparticles and its photocatalytic activity for Methyl orange
323 degradation, *Journal of Materials Science: Materials in Electronics*, **31**, 11303–11316.
- 324 Behzadi S., Nonahal B., Royae S.J. and Asadi A.A. (2020), TiO₂/SiO₂/Fe₃O₄ magnetic nanoparticles
325 synthesis and application in Methyl orange UV photocatalytic removal, *Water Science and
326 Technology*, **11**, 2432–2445.
- 327 Channei D., Inceesungvorn B., Wetchakun N. and Phanichphant S. (2014), Synthesis of
328 Fe₃O₄/SiO₂/CeO₂ core-shell magnetic and their application as photocatalyst, *Journal of
329 Nanoscience and Nanotechnology*, **14**, 7756–7762.
- 330 Chen F., Yan F., Chen Q., Wang Y., Han L., Chen Z. and Fang S. (2014), Fabrication of
331 Fe₃O₄@SiO₂@TiO₂ nanoparticles supported by graphene oxide sheets for the repeated
332 adsorption and photocatalytic degradation of rhodamine B under UV irradiation, *Dalton
333 Transactions*, **43**, 13537–13544.
- 334 Chen X., Wu Z., Liu D. and Gao. (2017), Preparation ZnO photocatalyst for the efficient and rapid
335 photocatalytic degradations of azo dyes, *Nanoscale Research Letters*, **12**, 143.
- 336 David P.S., Karananithi A. and Fathima N.N. (2020), Improved filtration for dye removal using
337 keratin-polymide blend nanofibrous membranes, *Environmental Science and Pollution
338 Research*, **27**, 45629–45638.
- 339 Dias N.C., Bassin J.P. and Sant'Anna G.L. (2019), Ozonation of the dye reactive red 239 and
340 biodegradation of ozonation products in a moving-bed biofilm reactor: revealing reaction
341 products and degradations pathways, *International Biodeterioration & Biodegradation*, **144**, 1–
342 9.

- 343 D'Amario L., Fohlinger J., Boschloo G. and Hammarstrom L. (2018), Unveiling hole trapping and
344 surface dynamics of NiO nanoparticles, *Chemical Science*, **9**, 223–230.
- 345 Elzahrani E. (2017), Photodegradation of binary azo dyes using core-shell Fe₃O₄/SiO₂/TiO₂
346 nanospheres, *American Journal of Analytical Chemistry*, **8**, 95–115.
- 347 Fu C., Liu X., Wang Y., Li L. and Zhang Z. (2019), Preparation and characterization of
348 Fe₃O₄@SiO₂@TiO₂-Co/rGO magnetic visible light photocatalyst for water treatment, *RSC*
349 *Advances*, **9**, 20256–20265.
- 350 Gao P., Liu J., Sun D.D. and Ng W. (2013), Graphene oxide-CdS composite with high photocatalytic
351 degradation and disinfection activities under visible light irradiation, *Journal of Hazardous*
352 *Materials*, **250**, 412–2420.
- 353 Gebrezgiabher M., Gebreslassie G., Gebretsadik T., Yeabyo G., Elemo F., Bayeh Y., Thomas M. and
354 Linert W. (2019), AC-Doped TiO₂/Fe₃O₄ nanocomposite for photocatalytic dye degradation
355 under natural sunlight irradiation, *Journal of Composites Science*, **3**, 75.
- 356 Girginova P.I., Daniel-da-Silva A.L., Lopes C.B., Figueira P., Otero M., Amaral V.S., Pereira E. and
357 Trindade T. (2010), Silica coated magnetite particles for magnetic removal of Hg²⁺ from water,
358 *Journal of Colloid and Interface Science*, **345**, 234–240.
- 359 Han J.S. and An G.S. (2021), Preparation of Dual-Layered Core–Shell Fe₃O₄@SiO₂ nanoparticles
360 and their properties of plasmid DNA purification, *Nanomaterials*, **11**, 3422.
- 361 Hariani P.L., Said M., Rachmat A., Riyanti F., Pratiwi H.C. and Rizki W.T. (2021), Preparation of
362 NiFe₂O₄ nanoparticles by solution combustion method as photocatalyst of congo red, *Bulletin of*
363 *Chemical Reaction Engineering & Catalysis*, **16**, 481–490.
- 364 Hariani P.L., Said M., Salni, Aprianti N. and Naibaho Y.A.L.R. (2022), High efficient photocatalytic
365 degradation of methyl orange dye in an aqueous solution by CoFe₂O₄-SiO₂-TiO₂ magnetic
366 catalyst, *Journal of Ecological Engineering*, **23**, 118–128.

- 367 Herman, J.M. (1995), Heterogeneous photocatalysis; an emerging discipline involving multiphase
368 system, *Catalyst Today*, **24**, 157–164.
- 369 Hosny N.M. (2011), Synthesis, characterization and optical band gap of NiO nanoparticles derived
370 from anthranilic acid and precursors via a thermal decomposition route, *Polyhedron*, **30**, 470–
371 476.
- 372 Hou C., Hu B. and Zhu J. (2018), Photocatalytic degradation of methylene blue over TiO₂ Pretreated
373 with varying concentrations of NaOH, *Catalysts*, **8**, 575.
- 374 Jarariya R. (2022), A review based on spinel ferrite nanomaterials MgFe₂O₄ - synthesis of
375 photocatalytic dye degradation in visible light response, *Journal of Environmental Treatment*
376 *Techniques*, **10**, 149–2156.
- 377 Kanakaraju D., Shahdad N.R.M., Lim Y. and Pace. A. (2018), Magnetic hybrid TiO₂/Alg/FeNPS
378 triads for the efficient removal of Methylene blue from water, *Sustainable Chemistry and*
379 *Pharmacy*, **8**, 50–62.
- 380 Kalam A., Al-Sehemi A.G., Assiri M., Du G., Ahmad T., Ahmad I. and Pannipara M. (2018),
381 Modified solvothermal synthesis of cobalt ferrite (CoFe₂O₄) magnetic nanoparticles
382 photocatalysts for degradation of Methylene blue with H₂O₂/visible light, *Results in Physics*, **8**,
383 1046–1053.
- 384 Khaki M.R.D., Shafeeyan M.S., Raman A.A.A. and Daud W.M.A.W. (2017), Evaluating the
385 efficiency of nano-sized Cu doped TiO₂/ZnO photocatalyst under visible light irradiation,
386 *Journal of Molecular Liquids*, **258**, 354–365.
- 387 Khan N.A., Saeed K., Khan I., Gul T., Sadiq M., Uddin A. and Zekker I. (2022), Efficient
388 photodegradation of orange II dye by nickel oxide nanoparticles and nanoclay supported nickel
389 oxide nanocomposite, *Applied Water Science*, **12**, 1–10.

- 390 Khodai M., Ghasemi N., Moradi B. and Rahimi M. (2013), Removal of methylene blue from
391 wastewater by adsorption onto ZnCl₂ activated corn husk carbon equilibrium studies, *Journal of*
392 *Chemistry*, **3**, 1–7.
- 393 Kotutha I., Duangchuen T., Swatsitang K., Meewasana W., Khajonrit J. and Maensiri S. (2019),
394 Electrochemical properties of rGO/CoFe₂O₄ nanocomposites for energy storage application,
395 *Ionics*, **25**, 5401–5409.
- 396 Kuang Y., Zhang X. and Zhou S. (2020), Adsorption of methylene blue in water onto activated carbon
397 by surfactant modification, *Water*, **12**, 587.
- 398 Lett J.A., Sagadevan S., Weldegebrical G.K. and Fatimah I. (2022), Hydrothermal synthesis and
399 photocatalytic activity of NiO nanoparticles under visible light illumination, *Bulletin of Chemical*
400 *Reaction Engineering & Catalysis*, **17**, 2, 340–349.
- 401 Lin J., Luo Z., Liu J. and Li, P. (2018), Photocatalytic degradation of methylene blue in aqueous
402 solution by using ZnO-SnO₂ nanocomposites, *Materials Science in Semiconductor Processing*,
403 **87**, 24–31.
- 404 Li Q., Lu C., Chen C., Xie L., Liu Y., Li Y., Kong Q. and Wang H. (2017), Layered NiCo₂O₄/ reduced
405 graphene oxide composite as an advanced electrode for supercapacitor, *Energy Storage*
406 *Materials*, **8**, 59–67.
- 407 Loan N.T.T, Hien Lan N.T.H, Hang N.T.T, Hai N.Q, Anh D.T.T, Hau V. T, Tan, L.V. and Tran T.V.
408 (2019), CoFe₂O₄ nanomaterials: effect of annealing temperature on characterization, magnetic,
409 photocatalytic, and photo-Fenton properties, *Processes*, **7**, 885.
- 410 Makeswari M. and Saraswathi, P. (2020), Photocatalytic degradation of methylene blue and methyl
411 orange from aqueous solution using solar light onto chitosan bi-metal oxide composite, *SN*
412 *Applied Sciences*, **2**, 336.

- 413 Moghaddam S.S., Moghaddam M.R.A. and Arami M. (2010), Coagulation/flocculation process for
414 dye removal using sludge from water treatment plant: optimization through response surface
415 methodology, *Journal of Hazardous Materials*, **175**, 651–657.
- 416 Moosavi S., Li R.Y.M., Lai C.W., Yusof Y., Gan S., Akbarzadeh O., Chowhury Z.Z., Yue X.G. and
417 Johan M.R. (2020), Methylene blue dye photocatalytic degradation over synthesized
418 $\text{Fe}_3\text{O}_4/\text{AC}/\text{TiO}_2$ nano-catalyst: degradation and reusability studies, *Nanomaterials*, **10**, 2360.
- 419 Ojemaye M.O., Okoh O.O. and Okoh A.I. (2017), Performance of $\text{NiFe}_2\text{O}_4\text{-SiO}_2\text{-TiO}_2$ photocatalyst
420 for the effective photocatalytic re-duction of Cr(VI) from aqueous solutions, *Journal of*
421 *Nanomaterials*, **2017**, 1–18.
- 422 Pham T.D., Bui T.T., Nguyen V.T., Bui T.K.V., Tran T.T., Phan Q.C., Pham T.D. and Hoang T.H.
423 (2018), Adsorption of polyelectrolyte onto nanosilica synthesized from rice husk: characteristics,
424 mechanisms, and application for antibiotic removal, *Polymers*, **10**, 220.
- 425 Prasad K.S. and Shamshuddin S.Z.M. (2022), Highly efficient conversion of glycerol and t-butanol
426 to biofuel additives over AIPO solid acid catalyst under microwave irradiation technique: kinetic
427 study, *Comptes Rendus Chimie*, **25**, 149–170.
- 428 Qiao H., Wei Z., Yang H., Zhu L. and Yan X. (2009), Preparation and characterization of NiO
429 nanoparticles by anodic arc plasma method, *Journal of Nanomaterials*, **2009**, 1–5.
- 430 Reman G.U., Tahir M., Goh P.S., Ismail A.F., Hafeez A. and Khan I.U. (2021), Enhancing the
431 photodegradation of phenol using $\text{Fe}_3\text{O}_4/\text{SiO}_2$ binary nanocomposite mediated by silane agent,
432 *Journal of Physics and Chemistry of Solids*, **153**, 110022.
- 433 Sadeghi S., Azhdari H., Arabi H. and Moghaddam A.Z. (2012), Surface modified magnetic Fe_3O_4
434 nanoparticles as a selective sorbent for solid phase extraction of uranyl ions from water sampels,
435 *Journal of Hazardous Materials*, **215**, 208–216.

- 436 Salomon R.V., Lydia I.S., Merlin J.P. and Venuvalingam P. (2012), Enhanced photocatalytic
437 degradation of azo dye using nano Fe₃O₄, *Journal of the Iranian Chemical Society*, **9**, 101–109.
- 438 Thy L.T.M., Cuong P.M., Tu T.H., Nam H.M., Hieu N.H. and Phong M.T. (2020), Fabrication of
439 magnetic iron oxide/graphene oxide nanocomposite for removal of lead ions from water,
440 *Chemical Engineering Transactions*, **78**, 277–282.
- 441 Vandevivere P.C., Bianchi R. and Verstraete W. (1998), Treatment and reuse of wastewater from
442 textile wet-processing industry: review of emerging technologies, *Journal of Chemical*
443 *Technology and Biotechnology*, **72**, 289–302.
- 444 Van Tran T., Nguyen D.T.C., Le H.T.N., Nguyen O.T.K., Nguyen V.H., Nguyen T.T., Bach L.G. and
445 Nguyen T.D. (2019), A hollow mesoporous carbon from metal-organic framework for robust
446 adsorbability of ibuprofen drug in water, *Royal Society Open Science*, **6**, 190058.
- 447 Vasiljevic Z.Z., Dojcinovic M.P., Vujancevic J.D., Jankovic-Castvan I., Ognjanovic M., Tadic N.B.,
448 Stojadinovic S., Brankovic G.O. and Nikolic M.V. (2020), Photocatalytic degradation methylene
449 blue, under natural sunlight using iron titanate nanoparticles prepared by a modified sol-gel
450 method, *Royal Society Open Science*, **7**, 1–15.
- 451 Wan X., Yuan M., Tie S. and Lan S. (2013), Effect of catalyst characters on photocatalytic activity
452 and process of NiO nanoparticles in the degradation of methylene blue, *Applied Surface Science*,
453 **277**, 40-46.
- 454 Wu Y., Shu R., Shan X., Zhang J., Shi J., Liu Y. and Zheng M. (2020), Facile design of cubic- like
455 cerium oxide nanoparticles decorated reduced graphene oxide with enhanced microwave
456 absorption properties, *Journal of Alloys and Compounds*, **817**, 152766.
- 457 Zhao P., Mo Z., Zhang P., Zhu X. and Guo R. (2015), Synthesis of graphene/Fe₃O₄/NiO magnetic
458 nanocomposites and its application in photocatalytic degradation the organic pollutants in
459 wastewater, *Journal of Porous Materials*, **22**, 1245–1253.

460 Ziaadini F., Mostafavia A., Shams pura T. and Fathirad F. (2019), Photocatalytic degradation of
461 Methylene blue from aqueous solution using $\text{Fe}_3\text{O}_4@\text{SiO}_2@\text{CeO}_2$ core-shell magnetic
462 nanostructure as an effective catalyst, *Advances in Environmental Technology*, **2**, 127–132.

463 Zielińska-Jurek A., Bielan Z., Dudziak S., Wolak I., Sobczak Z., Klimczuk T., Nowaczyk G. and
464 Hupka J. (2017), Design and application of magnetic photocatalysts for water treatment. The
465 effect of particle charge on surface functionality, *Catalysts*, **7**, 360.

466 Zinatloo-Ajabshir S. and Salavati-Niasari M. (2019), Preparation of magnetically retrievable
467 $\text{CoFe}_2\text{O}_4@\text{SiO}_2@\text{Dy}_2\text{Ce}_2\text{O}_7$ nanocomposites as novel photocatalyst for highly efficient
468 degradation of organic contaminants. *Composites Part B: Engineering*, **174**, 106930.

469

470

ACCEPTED MANUSCRIPT